Predicting nucleation textures in interstitial-free steel

Combined effect of oriented nucleation theory and strain-induced boundary migration

Ochoa-Avendaño, J.; Bos, C.; Kestens, L. A.I.

DOI
10.1016/j.commatsci.2025.113821

Publication date
2025

Document Version
Final published version

Published in
Computational Materials Science

Computational Materials Science 253 (2025) 113821

Contents lists available at ScienceDirect

Computational Materials Science

journal homepage: www.elsevier.com/locate/commatsci

Full length article

Predicting nucleation textures in interstitial-free steel: Combined effect of oriented nucleation theory and strain-induced boundary migration

J. Ochoa-Avendaño [a,*], C. Bos [a,b], L.A.I. Kestens [a,c]

[a] Department of Materials Science and Engineering, Delft University of Technology, Mekelweg 2, Delft, 2628 CD, Zuid-Holland, Netherlands
[b] Tata Steel Research & Development, P.O. Box 10000, IJmuiden, 1970 CA, Noord-Holland, Netherlands
[c] Metal Science and Technology, Department of Electromechanical, Systems and Metal Engineering, Ghent University, Technologiepark 46, IJmuiden, B-9052, Oost-Vlaanderen, Belgium

ARTICLE INFO

Keywords:
Crystallographic texture
Nucleation
Primary recrystallisation
Strain Induced Grain Boundary Migration
IF-steel

ABSTRACT

The accuracy of simulated recrystallisation textures is essential for predicting the formability of steel sheets. In a continuum modelling approach, this texture can be effectively calculated in two stages: nucleation and growth. However, the precision of the final texture depends heavily on the accuracy of the nucleation texture simulation. This paper presents a nucleation texture model that combines the strain-induced boundary migration (SIBM) mechanism with a traditional oriented nucleation model. The results indicate that the SIBM mechanism promotes the nucleation of low-stored energy grains and enhances the nucleation texture compared to using the oriented nucleation model alone. The findings suggest that the accuracy of nucleation texture could be improved by setting a minimum stored energy threshold for grains that nucleate during the early stages of recrystallisation.

1. Introduction

Steel sheets show a variety of mechanical properties determined by their microstructural characteristics. These features result from solid-state transformations that occur during the manufacturing process involving thermomechanical treatments. In the case of Interstitial-Free (IF) steel for forming applications, after hot rolling, the sheets undergo cold rolling followed by an annealing treatment to attain the desired formability properties. Various technological parameters, such as chemical composition, reheating temperature, hot roll finish temperature, cooling temperature, cold roll reduction, and subsequent annealing temperatures, affect the resulting microstructure of the finished sheet product [1,2]. The crystallographic texture is a crucial microstructural characteristic that needs to be controlled during thermomechanical processing. An appropriate recrystallisation texture resulting from the annealing treatment is crucial for the desired formability properties, assessed through the Lankford R-values [3].

During the annealing process applied on the cold rolled steel sheets, microstructural transformations take place. These transformations result from the rearrangement and annihilation of crystal defects, which reduce the plastically stored energy from the rolling process. This reduction in energy leads to the formation of subgrains with decreased dislocation density with respect to adjacent subgrains, which therefore may act as nuclei for the ensuing recrystallisation process. When high-mobility, large-angle grain boundaries surround such nuclei, subgrain boundary migration will occur and the dislocation free nucleus will invade the surrounding deformed matrix, which is the essence of a phenomenon commonly known as primary recrystallisation [4]. Therefore, nucleation is the initial phase of primary recrystallisation, marked by the emergence of nuclei. The nucleation texture denotes the crystallographic orientation distribution of these nuclei.

Various researchers have developed models to predict recrystallisation textures based on statistical mean-field approaches. Unlike topologically resolved full-field models, where the spatial character of the microstructural state variables are carefully accounted for, the mean-field models consider microstructural state variables in a statistical manner [5,6]. In this context, the crystallographic texture of the material is represented by the orientation distribution function (ODF), $f(g)$, which associates each crystallographic orientation g with the volume fraction of crystals in the specimen. In a very simplified approach, according to the above mentioned description whereby the static recrystallisation texture is essentially considered as the result of sequential nucleation and growth phenomena, the recrystallisation texture $f_R(g)$ can be represented as follows:

$$f_R(g) = c_1 P_G(g)(c_2 P_N(g) f_D(g)). \quad (1)$$

* Corresponding author.
E-mail address: J.F.OchoaAvendano@tudelft.nl (J. Ochoa-Avendaño).

https://doi.org/10.1016/j.commatsci.2025.113821
Received 21 November 2024; Received in revised form 2 March 2025; Accepted 3 March 2025
Available online 19 March 2025

whereby, $f_D(g)$ is the Orientation Distribution Function (ODF) of the deformed material, $P_N(g)$ represents the orientation dependent nucleation probability distribution and $P_G(g)$ represents the orientation dependent growth probability distribution. The normalisation constant c_1 is determined by the condition that $\int f_R(g)dg = 1$. The product $c_2 P_N(g) f_D(g)$ yields the nucleation texture $f_N(g)$, whereby the normalisation constant c_2 is determined by the condition that $\int f_N(g) = 1$.

A model that implements Eq. (1) is the Kestens–Jonas (K–J) model, which was applied on IF steel [7], electrical steel [8] and aluminium alloys [9]. This model can simulate the evolution of a deformation texture, represented by a discrete set of orientations or a continuous function, either obtained through crystal plasticity models or from experimental observation. The approach, based on Eq. (1) is of a statistical nature, whereby it is assumed that nuclei orientations are selected among deformed orientation according to a given nucleation probability $P_N(g)$. Equally, the growth rate of these nuclei in the deformed matrix is approximated by a growth probability $P_G(g)$ operating on the nucleation texture $f_N(g)$. Both nucleation and growth probabilities $P_N(g)$ and $P_G(g)$ are based on physical grounds, depending on the precise nucleation or growth mechanism under consideration [7]. It needs to be emphasised that in this approach only the crystallographic features of recrystallisation are considered whereby other features such as kinetics, morphological (grain size or aspect ratio) and topological aspects are ignored. Despite the drastic simplification, the results obtained with the Kestens–Jonas model are meaningful and low-demanding in computational cost [10].

In the K–J model applied to IF-steel it is assumed that nucleation predominantly occurs within matrix grains with high stored energy [7]. Nevertheless, this premise is challenged by experimental studies demonstrating that nuclei can also emerge in areas characterised by significantly lower stored energy [11]. Research indicates that this phenomenon can be attributed to the activation of the Strain-Induced Boundary Migration (SIBM) mechanism [12], a process initially identified by Beck and Sperry in high-purity aluminium [13]. The SIBM process involves the outward bulging of an existing grain boundary within deformed microstructures [14], driven by gradients in stored energy across the grain boundary.

The modelling of the nucleation texture $f_N(g)$ is crucial for accurate recrystallisation texture modelling. Therefore, improving this module in the Kestens–Jonas (K–J) model offers significant potential to increase its accuracy. This study introduces the Strain-Induced Boundary Migration (SIBM) nucleation mechanism into the K–J model to determine the impact of SIBM on the formation of the nucleation texture. The research focuses on interstitial-Free (IF) steel that has undergone 80% cold rolling reduction, followed by a 30 min annealing treatment at 630 ° C. This treatment is designed to produce a low volume fraction of early recrystallised grains, which can be considered representative of the nucleation texture. The results of this approach are compared with experimental data, with a discussion focusing on the discrepancies between the simulated and the experimentally measured nucleation texture. Furthermore, the study includes an analysis of the location of nuclei in the orientation space and how this location is influenced by the deformation texture used as input for the nucleation texture modelling.

2. Materials and methods

2.1. Modelling methods

2.1.1. Continuum modelling of recrystallisation textures

As mentioned in the introduction, the continuum modelling of recrystallisation textures is based on a statistical approach whereby distribution functions of microstructural state variables are considered, implying that the topological aspects of the microstructure are either statistically considered or partially neglected [5,6]. The basic formula for this modelling approach is given in Eq. (1).

The nucleation texture $f_N(g)$ is the result from the operation of the nucleation probability function $P_N(g)$ on the deformation texture $f_D(g)$:

$$f_N(g) = P_N(g) f_D(g). \tag{2}$$

$P_N(g)$ is the probability of nucleation of crystal orientations in the deformed matrix, and $f_D(g)$ is the deformation texture representing the ODF of the deformed material. In a through-process continuum modelling approach, $f_D(g)$ is calculated with a mean-field crystal plasticity model. In this research, the Advanced-Lamel model (ALAMEL) has been selected for modelling the deformation texture, cf. Section 2.1.2. This model has demonstrated the capability to predict deformation textures with moderate to high accuracy at a very low computational cost [15]. Additionally, the ALAMEL model incorporates grain interaction during plastic deformation through a pairwise arrangement of grains, making it well-suited for the implementation of the SIBM nucleation mechanism, cf. Section 2.1.5.

2.1.2. Advanced-Lamel model

The Advanced-Lamel (ALAMEL) model by Van Houtte et al. [16] is a crystal plasticity mean-field model capable to predict the deformation texture of a polycrystal undergoing plastic deformation. The model operates on a discrete set of orientations by assuming a pairwise organised assembly, where each pair is randomly linked to an orientation vector $\vec{\boldsymbol{V}}_{\boldsymbol{GB}}$ representing the normal to a virtual grain boundary plane separating the two orientations, cf. Fig. 1. This approach allows for accounts for the interaction between neighbouring orientations in a statistically averaged manner. Further details on the ALAMEL model methodology are available in the work of Van Houtte et al. [16].

In this study the ALAMEL model is applied to simulate the cold-rolling process with a reduction of 80%. The initial texture for the simulation was derived from a set of 5000 orientations based on the experimentally measured texture of the as-received material shown in Fig. 6(*a*). The discrete set of orientations was obtained by applying the so-called STAT method by Toth and Van Houte [17]. The simulation was carried out under plane strain conditions with a strain amplitude (ε) of 1.60 and a strain rate ($\dot{D}_0$) of 0.01 s^{-1}. Twenty-four slip systems $\{110\}\langle 111\rangle$ and $\{112\}\langle 111\rangle$ were considered, whereby all slip systems are assumed to exhibit equal critical resolved shear stress. Ideal plasticity was assumed, i.e. strain hardening was not considered in the simulation. Further details on the ALAMEL rolling simulation can be found in [15], additionally, Appendix A provides the deformation texture evolution using ALAMEL model.

2.1.3. Nucleation in Kestens–Jonas model

Assuming that $f_D(g)$ is the ODF of the deformed material and $P_N(g)$ is the nucleation probability distribution. The normalised nucleation texture will be given by:

$$f_N(g) = \frac{P_N(g) f_D(g)}{\int_\Omega P_N(g) f_D(g) \mathrm{d}g}. \tag{3}$$

whereby the integral in Eq. (3) covers the entire orientation space Ω.

According to Kestens and Jonas [7], the nucleation texture appearing in the initial stages of recrystallisation after cold rolling to reductions in the range of 70 to 90% is controlled by the so called high stored energy mechanism. This implies that recrystallisation nuclei appear in areas of the microstructures with increased levels of slip activity, which generally selects the $\gamma - fibre$ grains ($\langle 111\rangle \parallel ND$) as they correspond to the higher Taylor factor grains as shown in Fig. 2, assuming that the Taylor factor $M(g)$ of a crystal orientation g is a representative measure of its slip activity during plastic deformation. The model simply posits that only orientations for nucleation are selected of which the Taylor factor exceeds a critical threshold M_0. In this approach we can assume the following explicit form for $P_N(g)$, which represents a logistic-type function:

$$P_N(g) = A[1 + \exp(-k_1 M(g) - M_0)]^{-1}. \tag{4}$$

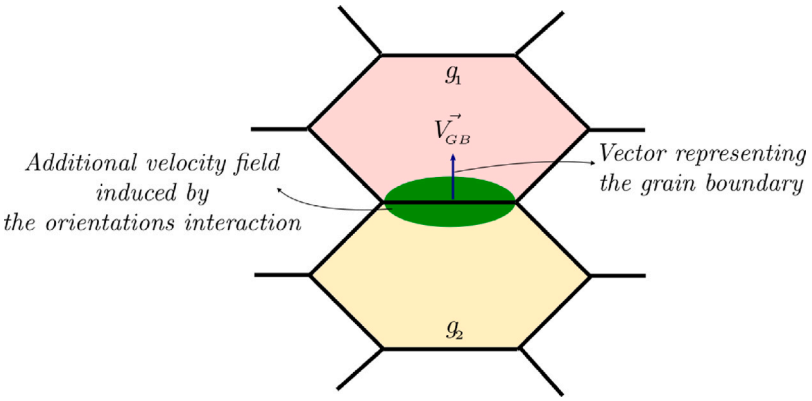

Fig. 1. ALAMEL model description, cluster assembly for texture evolution calculation.

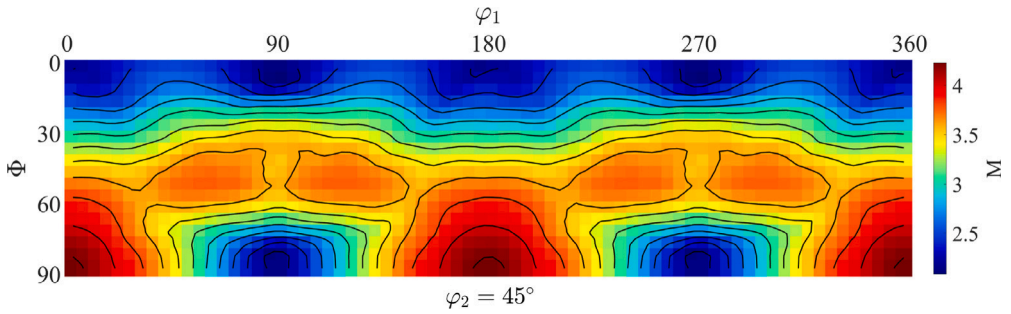

Fig. 2. Taylor factor distribution in Euler space according to FCT model for BCC material submitted to plain strain compression.

whereby $M(g)$ is the Taylor factor of the orientation g, and k_1 describes the steepness of the function $P_N(g)$. A is the normalisation factor such that $\int f_N(g)dg = 1$. It can be shown that:

$$A^{-1} = \frac{1}{k_1}\left[\ln\frac{1+\exp(k_1 M(g) - M_0)}{1+\exp(-k_1 M(g) - M_0)}\right]. \tag{5}$$

The nucleation texture defined in Eq. (3) incorporating $P_N(g)$ as defined in Eq. (4) will be referred to as Nucleation Rule I (NR-I) in this research:

$$f_N^{\mathrm{I}}(g) = \frac{P_N(g) f_D(g)}{\int_\Omega P_N(g) f_D(g)\mathrm{d}g}. \tag{6}$$

2.1.4. The Taylor factor

The crystal plasticity theory allows to express the Taylor factor M as a dimensionless measure of the plastic power dissipated [2,11]; it can be defined as:

$$M = \sum_{(s)} \frac{|\mathrm{d}\gamma^{(s)}|\tau_{crrs}}{\sigma_0 \mathrm{d}\varepsilon_{VM}}. \tag{7}$$

where $\sum_{(s)}|\mathrm{d}\gamma^{(s)}|$ is the total instantaneous slip increment on the slip system (s), τ_{crrs} the critically resolved shear stress, σ_0 the external stress applied, and ε_{VM} the von Mises equivalent strain. M can be derived from crystal plasticity simulations [7]. For example, for a BCC material submitted to plane strain compression conditions, the Full-Constrain Taylor (FCT) model allows the Taylor factor M to be determined for an arbitrary crystal orientation g, such that the function $M(g)$ can be derived, cf. Fig. 2.

The proposed nucleation probability distribution described in Eq. (4), will suppress nucleation for orientations with a Taylor factor below a specified threshold value M_0. Correspondingly, cf. Fig. 2, orientations in the vicinity of the $\theta - fibre$ (with $\langle 001\rangle \parallel ND$) will be suppressed in this model, whereas $\gamma - fibre$ orientations (with $\langle 111\rangle \parallel ND$) will be enhanced by this nucleation operator.

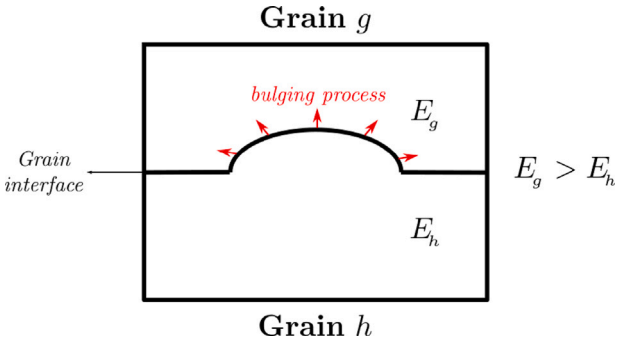

Fig. 3. Representation of SIBM nucleation in a pair of grains (g,h), Grain g is being replace by Grain h, since dislocation density is higher in Grain g.

2.1.5. SIBM nucleation based on ALAMEL model

The mechanism of strain-induced grain boundary migration (SIBM), initially documented by Beck and Perry [13], involves the formation of new recrystallisation nuclei by bulging out of an existing grain boundary [18]. This process is driven by the difference in plastically stored energy across the interface. As a result, the boundary moves into the more deformed grain, increasing the volume of the crystal orientation with lower stored energy, as illustrated in Fig. 3. The pursuit of equilibrium produces the replacement of grains with high dislocation content (grain g) by grains with low dislocation content (grain h) [13]. At this point, it is important to clarify that in the context of continuum texture modelling, and consequently in this study, g and h represent crystallographic orientations, which are treated as individual grains for the purposes of the implementation described here.

As discussed in Section 2.1.2, the ALAMEL model operates on a set of crystal orientations in which the velocity gradient is accommodated not by each single orientation as in the Full-Constrain Taylor model, but by a pair of grains. To this purpose the assembly of N orientations

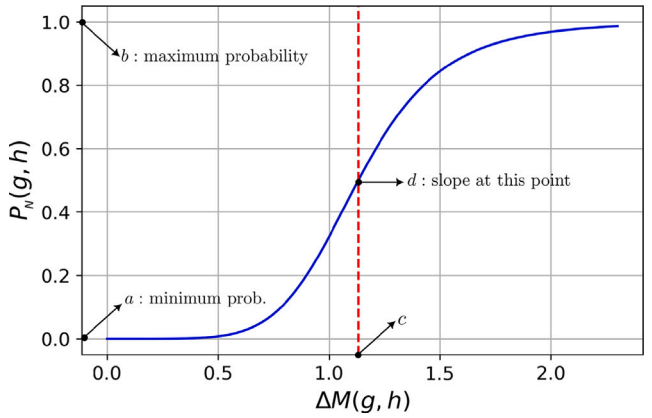

Fig. 4. $P_N(g,h)$ from SIBM nucleation model, cf. (8). Nucleation probability as function of the difference between Taylor factor for a pair of grains h and g $|\Delta M_{(g,h)}|$.

is randomly grouped in $N/2$ pairs (N is even). Although the ALAMEL model does not explicitly take into account the topology of the local microstructure, the pairwise approach implicitly accounts for local interactions between two grains. Crystal orientations are considered in pairs, which jointly comply with the boundary conditions of the externally imposed velocity field, but which can relax constraints by allowing an equal but opposite shear in the virtual grain boundary plane that separates the two orientations. Consequently, the plastically dissipated energy in a crystal orientation depends on the adjacent orientation with which it is paired. Thus, it is feasible to formulate a nucleation operator based on the SIBM mechanism for a pair of grains (g,h). In this study, the SIBM nucleation probability within a pair of grains is denoted as $P_N(g,h)$.

The absolute value of the stored energy difference in a pair of grains (g,h) is expressed as $|\Delta E(g,h)|$. Therefore, the nucleation probability in this pair of grains $P_N(g,h)$ can be derived from the so-called four-parameter logistic equation ($4PL$) [19] as:

$$P_N(g,h) = \frac{a-b}{1+\left(\frac{|\Delta E(g,h)|}{c}\right)^d} + b. \tag{8}$$

where:

- a : minimum probability value taken by $P_N(g,h)$. For the purpose of this work $a = 0$ indicating no SIBM nucleation probability.
- b : maximum probability value taken by $P_N(g,h)$. For the purpose of this work $b = 1$, indicating full SIBM nucleation probability.
- c : the point of inflection on the half-way of $P_N(g,h)$.
- d : Slope of the curve at the point c.

The SIBM nucleation probability presented in Eq. (8) is plotted in Fig. 4, with the parameters a, b, c, and d shown.

Similarly to the nucleation operator introduced in Eq. (4), the stored energy can be approximated using the Taylor factor, denoted as $M(g)$ in Eq. (8). Hence, for two grains pairwise deformed in the ALAMEL model simulation, the difference in stored energy is assumed to be proportional to $|\Delta M(g,h)|$. In addition to the energetic conditions, the SIBM mechanism requires a high-angle grain boundary (HAGB) between the pair of grains (g,h), which has been reported to foster the grain boundary mobility [20]. Therefore, $P_N(g,h)$ returns a non-zero value only for pairs of grains that share a HAGB, i.e. $\Delta(g,h) \geq \theta_0$, whereby $\Delta(g,h)$ represents the misorientation angle between the grains g and h. Hence, Eq. (8) turns into:

$$P_N(g,h) = \begin{cases} \frac{-1}{1+\left(\frac{|\Delta M(g,h)|}{c}\right)^d} + 1 & \text{if} \quad \Delta(g,h) \geq \theta_0. \\ 0 & \text{otherwise.} \end{cases} \tag{9}$$

Table 1
Chemical composition of the IF-Steel used in this study.

	C	Mn	Ti	N	Al
wt.[%]	0.002	0.13	0.065	0.004	0.05

Table 2
IF-steel samples used in this study.

Sample name	Cold rolling reduction (%)	Heat treatment Temperature (°C)	Heat treatment Time (min)
S_0	80	–	–
S_1	80	630	30

Fig. 3 displays the SIBM nucleation mechanism in the case where $E(g) > E(h)$, resulting in grain h bulging into grain g. However, the reverse scenario unfolds if $E(g) < E(h)$, with grain g bulging into the grain h. Both potential scenarios can arise when nucleation is analysed for an ALAMEL pair of grains: first, when grain h nucleates, and second, when grain g nucleates. Applying Eq. (2), the nucleation texture by SIBM mechanism for a set of grains organised by pairs (g,h) can be derived as follows in each respective case:

$$f_N^{\mathrm{II}}(g) = k_2 P_N(g,h) f_D(g). \tag{10}$$

whereby g corresponds to the orientation with minimum Taylor factor of the pair, such as $min(M(g), M(h))$. k_2 is a normalisation factor to ensure $\int f_N^{\mathrm{II}} = 1$. The superscript II, indicates a second nucleation rule defined in this paper, referred to hereinafter as NR-II.

2.1.6. Nucleation rules combined

The combination of the nucleation rules NR-I and NR-II, defined by Eqs. (6) and (10) respectively, is achieved by balancing their influence on the overall nucleation texture in Eq. (11). It is important to clarify that this operation is feasible only when both $f_N^{\mathrm{I}}(g)$ and $f_N^{\mathrm{II}}(g)$ have been normalised separately to ensure $\int f_N(g)dg = 1$.

$$f_N(g) = k_3(\Gamma f_N^{\mathrm{I}}(g) + (1-\Gamma) f_N^{\mathrm{II}}(g)). \tag{11}$$

In this case, Γ and $(1-\Gamma)$ are the weighting factors for the high stored energy and the SIBM nucleation mechanisms, respectively. Γ varies in the interval $[0,1]$, and k_3 again serves as normalisation factor.

2.2. Experimental methods

2.2.1. Material and thermomechanical treatments

A plate of hot-rolled IF-steel ($thickness$ = 5 mm, $width$ = 60 mm) with the chemical composition provided in Table 1 was used in this study. The as-received plate was cold rolled on a laboratory mill, achieving 80% reduction in thickness. Two samples were extracted: sample S_0, representing the deformed state, and sample S_1, which, underwent an annealing treatment as outlined in Table 2. The sample S_1 embodies the very early recrystallised state which is considered the nucleation state in this study.

The samples were analysed using the Electron Backscatter Diffraction (EBSD) method, with the plane of observation parallel to the ND-RD plane and close to the centre of the sheet. The preparation of these surfaces for EBSD scanning included the use of OPS solution and electropolishing techniques. These EBSD scans were recorded with a FEI Quanta 450 scanning electron microscope equipped with the EDAX-TSL® acquisition system using the EDAX-APEX™ software. The tilt angle for the specimens was set at 70°, and the areas scanned were rectangular with $width$ = 500 μm and $length$ = 200 μm, employing a step size of 0.7 μm on a hexagonal grid.

2.2.2. Recrystallised fraction partitioning

The EBSD data of sample S_1 was processed to distinguish between recrystallised and deformed-matrix grains. There is no universally accepted method for this differentiation, making the process subjective due to the lack of a clear definition of a grain [21]. Previous studies have approached this task by using criteria derived from EBSD data, including the Image Quality (IQ) of diffraction patterns [22,23] or internal misorientation indicators such as Grain Orientation Spread (GOS) and Kernel Average Misorientation (KAM) [23–26]. Furthermore, some methods also consider morphological features of the microstructure, focusing on grain size (GSZ) and geometrical characteristics such as grain aspect ratio [27]. For a comprehensive introduction on the application of EBSD metrics, readers are encouraged to consult the documentation provided by the MTEX software [28].

The present study employs a combination of three parameters to identify recrystallised grains: the grain size in terms of area GSZ_A [μm^2], the GOS [°], and a ratio of the two GOS/GSZ_A. The first rationale behind this approach was to identify grains with low internal misorientation, as indicated by low GOS values, a method extensively adopted in prior research [24,26]. However, non-recrystallised grains, especially smaller ones, may also present low GOS values due to the small amount of scanned points considered in the GOS calculation. To enhance the metric's accuracy, an additional criterion of minimum GSZ_A threshold was added to refine the low GOS criterion. Despite the GSZ_A correction, some grains that are large enough and exhibit low internal orientation gradients can mistakenly be classified as recrystallised due to low GOS and relatively large GSZ_A. Therefore, the GOS/GSZ_A ratio is considered to exclude non-recrystallised grains that have low, but not minimal GOS values. This ratio criterion combined with GOS and the GSZ_A criteria, cf. Eq. (12), was applied to partition the early recrystallised grains.

$$(GSZ_A > 2.5\ \mu m^2) \wedge (GOS \leq 2.50°) \wedge (GOS/GSZ_A \leq 0.1°/\mu m^2). \quad (12)$$

The analysis of the EBSD data was conducted using MTEX software [29]. For grain reconstruction, a grain boundary angle threshold of 5° was used. The critical values on Eq. (12) were selected by visual inspection of the orientation scans.

2.2.3. Macro-texture analysis

Data from EBSD scans were utilised to compute the Orientation Distribution Functions (ODFs) based on individual orientations defined by Euler angles $g = \{\varphi_1, \Phi, \varphi_2\}$. These ODFs were derived based on the generalised harmonic series expansion method, as suggested by Bunge [30] with $l_{max} = 22$. On every pixel in the EBSD scan, a Gaussian ODF with a 7° spread was centred, and the superposition of these Gaussian functions provided the overall ODF. The ODFs were calculated using MTEX software without any assumptions of sample symmetry [29]. The resulting ODFs are presented in the traditional $\varphi_2 = 45°$ sections calculated in the triclinic domain, i.e. with $0° < \varphi_1 < 360°$ and $0° < \Phi, \varphi_2 < 90°$. Fig. 5 illustrates the positions of the crystallographic components and the fibres examined in this paper.

The similarity between textures compared throughout this research was measured using the texture correlation index J_D. This index, featured in the ATEX software [31], varies from 0.0 to 1.0. A value of 1.0 signifies a perfect correlation between the two compared ODFs, whereas a value of 0.0 indicates no correlation whatsoever. The Eq. (13) shows how the index J_D is defined for two ODFs $f_A(g)$ and $f_B(g)$ being compared.

$$J_D = \frac{\int_g f_A(g) f_B(g) \mathrm{d}g^2}{\sqrt{\int_g f_A^2(g) \mathrm{d}g^2 \cdot \int_g f_B^2(g) \mathrm{d}g^2}}. \quad (13)$$

3. Results

3.1. Deformation textures

Fig. 6(a) presents the texture used as input for the ALAMEL rolling simulation. The ODF was obtained by discretising the measured ODF on the hot rolled IF-steel sheet in as-received condition in a sample of 5000 discrete orientations. The texture is a typical transformation type texture resulting from the austenite-to-ferrite transformation after hot rolling. It exhibits a maximum of 2.6 on the rotated cube component ($i.e.\{001\}\langle 110\rangle$), whereby also the $\gamma - fibre$ is present, albeit with low intensities.

Fig. 6(b) shows the ODF of the sample S_0 corresponding to the experimental deformation texture derived from EBSD experiments. This texture mainly displays the $\alpha - fibre$ and $\gamma - fibre$ development, as expected for a BCC material submitted to a medium-to-high rolling reduction [2]. The simulated deformation texture obtained by the ALAMEL model as explained in Section 2.1.2 is presented in Fig. 6(c). Similarly to the experimental deformation texture, the $\alpha - fibre$ and $\gamma - fibre$ are also present in the simulated texture, although with higher intensities. Though the ALAMEL prediction generally aligns well with the experimentally measured deformation texture presented in Fig. 6(b), the latter exhibits more balanced intensity distributions between the α and γ fibres than the ALAMEL simulated texture. Contrary to the experimental deformation texture, where the strongest components of $\alpha - fibre$ are the $\{001\}\langle 110\rangle$ and $\{112\}\langle 110\rangle$ components, the ALAMEL simulation displays the maximum intensity at the $\{113\}\langle 110\rangle$ component. In general, the simulated texture overemphasises orientation rotations compared to the experimentally observed texture, a well-known characteristic of crystal plasticity mean-field texture predictions [15,18,32].

3.2. Nucleation state and experimental nucleation texture

The EBSD data of sample S_1 was processed to isolate the recrystallised grains as detailed in Section 2.2.2. Fig. 7(a) shows the inverse pole figure (IPF) map of all the data, while Fig. 7(b) displays the early recrystallised grains corresponding to ~12% of recrystallised fraction, and for the purpose of this study, that will be considered as the grains that have nucleated.

Fig. 7(c) presents the ODF for sample S_1, which includes both recrystallised and non-recrystallised grains, representing the overall texture of the microstructure depicted in Fig. 7(a). The texture displays both the α and γ fibres, which was expected considering that ~88% of the grains have not yet recrystallised. However, the presence of ~12% of recrystallised grains, assumed here as nuclei, appears to make the α and γ fibres less homogeneous when compared with the experimental deformation texture shown in 6(b). Notably, components such as $\{113\}\langle 110\rangle$ and ~$\{111\}\langle 121\rangle$ are observed.

Fig. 7(d) shows the ODF of the recrystallisation nuclei of sample S_1, corresponding to the coloured grains depicted in Fig. 7(b). This texture predominantly shows a significant development of the $\gamma - fibre$ with a maximum intensity of a component with Euler angles ($\varphi_1 = 45°, \Phi \approx 54°, \varphi_2 = 45°$). Additionally, some crystallographic components appear in the Euler space region where $0° < \Phi < 45°$, including crystallographic components located on the $\theta - fibre$, characteristics previously observed by Ayad et al. [21].

3.3. Simulation parameters selection

The two nucleation rules defined in this study, NR-I cf. Eq. (6) and NR-II cf. Eq. (10), along with their combined form, Eq. (11), incorporate parameters that need to be specified for nucleation texture simulations. Multiple simulations were conducted using different parameter combinations, as outlined in Table 3.

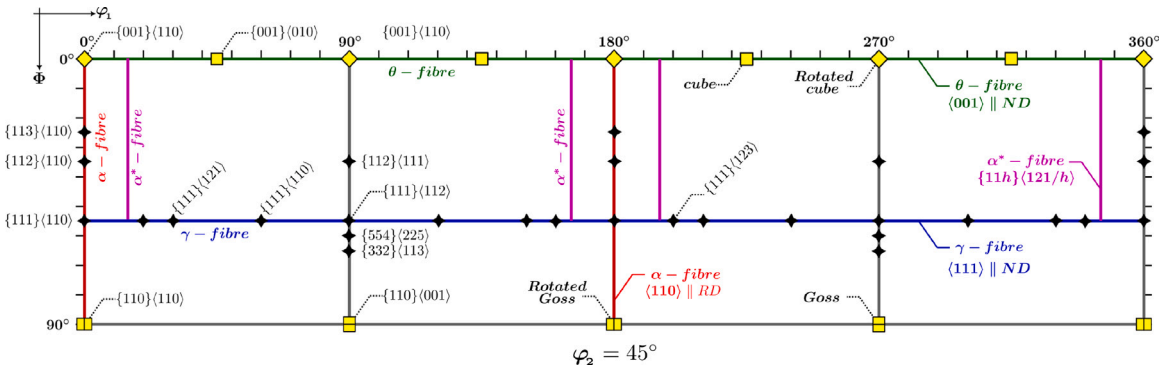

Fig. 5. Relevant fibre textures and crystallographic components for textures analysis in BCC alloys for rolling and annealing textures; $\varphi_2 = 45°$ section.

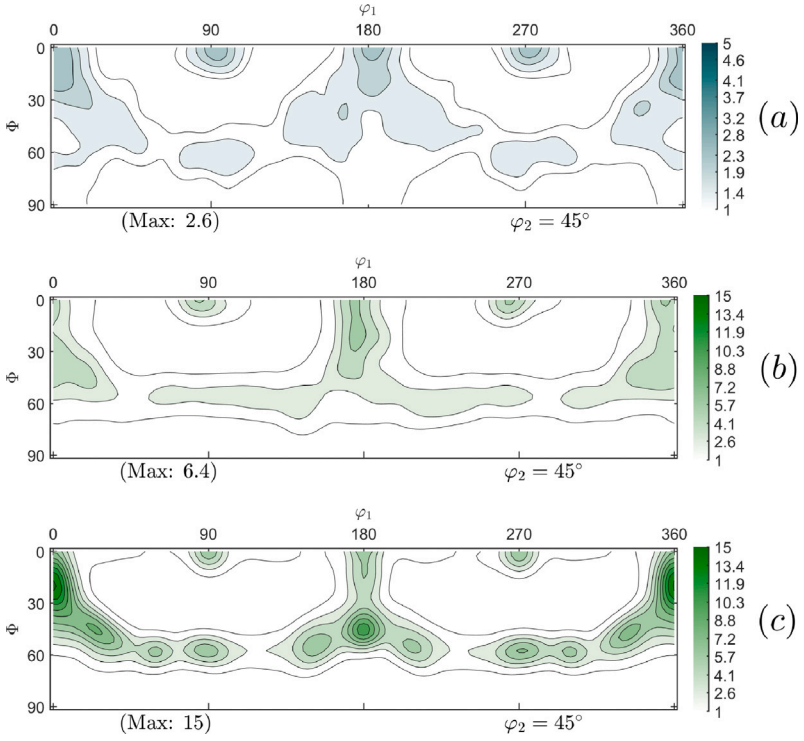

Fig. 6. (*a*) Input texture for the ALAMEL rolling simulation corresponding to a 5000 orientations discretisation of the experimentally measured texture of the as-received material. (*b*) Experimental deformation texture obtained by EBSD data from sample S_0. (*c*) Simulated deformation texture calculated with ALAMEL model 80% reduction.

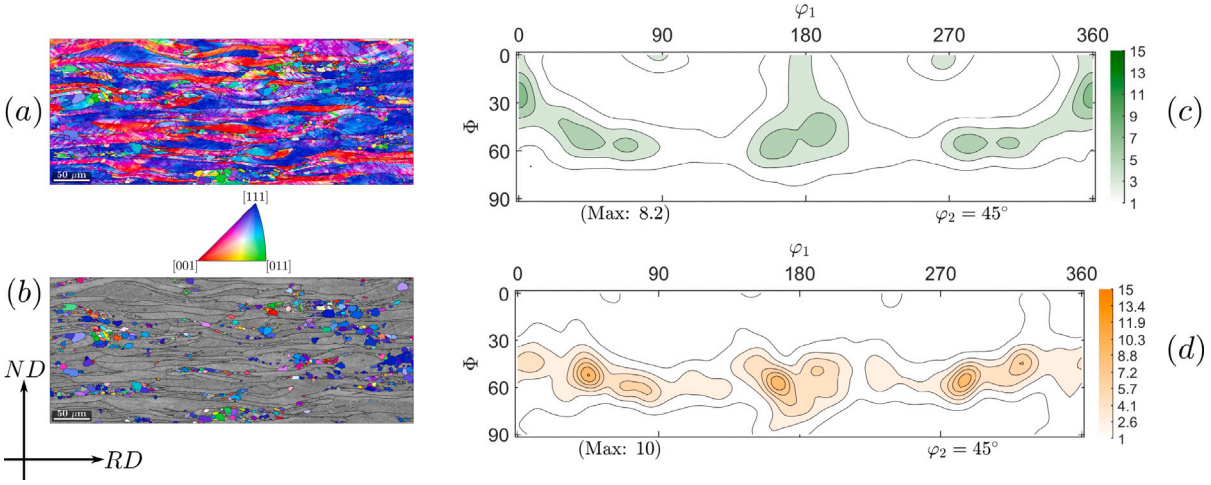

Fig. 7. IPF-map of the sample S_1, (*a*) all data and (*b*) early recrystallised grains. (*c*) Texture of the sample S_1 all grains (*d*) early recrystallised grains corresponding to the experimental nucleation texture in this study.

Table 3
Parameters defined to carry out nucleation texture simulations.

Equation	Parameters to be defined	Values selected
NR-I Depends mainly on $P_N(g)$	M_0: Threshold of Taylor factor.	For $M(g)$ frequency distribution: $M_0 = [30, 40, 50, 60, 70, 80, 90]th - percentile$
	k_1: Steepness of $P_N(g)$ probability function.	$k_1 = 1.0$
NR-II Depends mainly on $P_N(g,h)$	c: Inflection point $P_N(g,h)$	For $M(g)$, $c = [\max(M(g)) - \min(M(g))]/2$
	d: Slope of $P_N(g,h)$ at point c.	$d = 6.0$
	θ_o: HAGB criterion	$\theta_o = 10.0°$
NR-I and NR-II combined	Γ: weighting factor for the combination of NR-I and NR-II.	$\Gamma = [0.1, 0.2, 0.3, 0.4, 0.5, 0.6, 0.7, 0.8, 0.9, 1.0]$

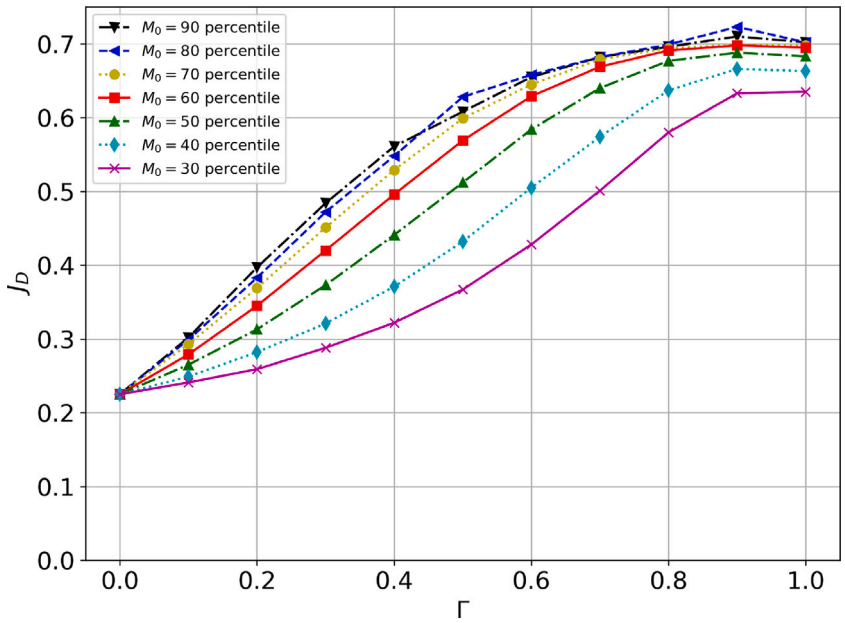

Fig. 8. J_D values calculated from comparing simulated nucleation textures using parameters listed in 3 with experimentally measured nucleation texture.

The simulated nucleation textures, generated using the parameters listed in Table 3, were compared with the experimentally determined nucleation texture shown in Fig. 7(*d*). The comparison was performed quantitatively using the texture correlation index J_D, as defined in Section 2.2.3. The resulting J_D values are presented in Fig. 8, where the vertical axis represents the calculated J_D, with 0.0 indicating no correlation between the compared textures and 1.0 indicating total correlation. The horizontal axis represents the weighting factors for the combination of NR-I and NR-II, as defined in Eq. (11). Specifically, $\Gamma = 0.0$ indicates no influence from NR-I and total influence from NR-II, while $\Gamma = 1.0$ indicates no influence from NR-II and total influence from NR-I.

Each curve in Fig. 8 represents a simulation batch where M_0 is kept constant, while the Γ parameter varies. The first notable characteristic in Fig. 8 is the critical role of M_0, which serves as a metric for plastic stored energy in this study and directly in the performance of the NR-I (cf. Eq. (6)). A general trend is observed: as M_0 increases, the simulated nucleation textures more closely resemble the experimental nucleation texture. However, the highest J_D value is achieved at $M_0 = 80th - percentile$. Additionally, Fig. 8 shows that higher Γ values, indicating a greater influence of NR-I, result in better texture correlation. However, in some simulation batches, reducing Γ and thereby increasing the influence of NR-II on the final nucleation texture produces improved J_D values.

According with Fig. 8, the highest texture correlation index among all the simulations performed is $J_D = 0.723$. This value was achieved by the nucleation texture combining NR-I and NR-II in a ratio of $9:1$, using $M_0 = 80th - quantile$ in NR-I. In this simulation, the individual application of NR-I resulted in $J_D = 0.702$, demonstrating good correlation with the experimental nucleation texture, while the individual application of NR-II resulted in $J_D = 0.225$, indicating no close correlation with respect to the experimental result. These results were selected for further analysis in the following section.

3.4. Simulated nucleation textures comparison

The experimental nucleation texture already detailed in Section 3.2 is brought back in Fig. 9(*a*) for comparison with the simulated ones. This ODF mainly exhibits nuclei oriented in the $\gamma - fibre$ region, with a notable peak at the $\{111\}\langle 123\rangle$ component. This observation is in agreement with previous studies, which have reported a reduction in the $\alpha - fibre$ components and an enhancement of the $\gamma - fibre$ during early stages of primary recrystallisation [21]. In general, the presence of $\gamma - fibre$ components is attributed to the preferred orientation of the nuclei, which is linked to their high stored energy [7,33].

Fig. 9(*b*) illustrates the nucleation texture obtained using NR-I (K–J model), calculated by applying Eqs. (6) and (4) with parameters $k_1 = 1.0$ and $M_0 = 80th - quantile$. This texture predominantly shows nucleation of crystallographic components on the $\gamma - fibre$, corresponding to orientations with medium-high Taylor factor values, as seen in Fig. 2. The strongest components in this texture are the $\{111\}\langle 123\rangle$ and the $\{554\}\langle 225\rangle$. Furthermore, it is noted that no $\theta - fibre$ components are forecasted, and only some low intensity components oriented near the $\alpha - fibre$ appear in the simulated texture. These observations reveal a discrepancy between the predictions of NR-I and the experimental ODF shown in Fig. 9(*a*).

The texture predicted by applying NR-II is displayed in Fig. 9(*c*). This texture was obtained by applying Eqs. (9) and Eq. (10) with parameters $a = 0.0$; $b = 1.0$; $c = [\max(M(g)) - \min(M(g))]/2$; $d = 6.0$ and $\theta_0 = 10.0°$, cf. Section 3.3. It mainly predicts nuclei with strong

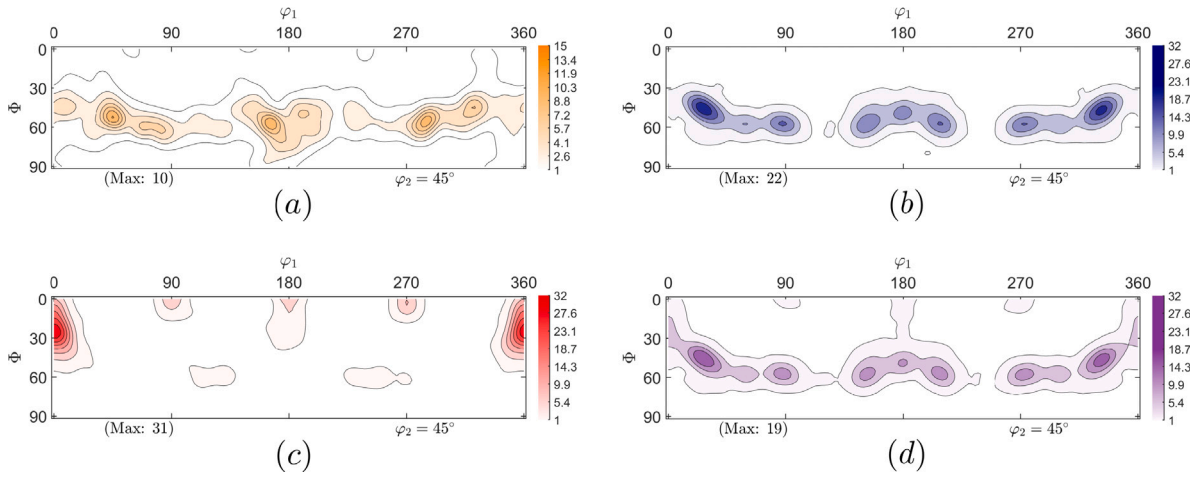

Fig. 9. (*a*) Experimentally measured nucleation texture obtained from EBSD data, cf. Section 3.2. (*b*) Predicted by K–J model, Eq. (6). (*c*) Predicted by SIBM nucleation model, Eq. (10). (*d*) Predicted combining K–J and SIBM nucleation models, Eq. (11).

intensities of crystallographic orientations in the $\alpha - fibre$, especially the $\{113\}\langle 110\rangle$ component, and fewer in the $\gamma - fibre$ with much lower intensities. The second nucleation rule NR-II stimulates the nuclei with low Taylor factor values, cf. Fig. 2. However, the absence of nuclei with high intensities in the $\gamma - fibre$ and the overestimation of $\alpha - fibre$ components indicate a deviation from the experimental nucleation texture shown in Fig. 9(*a*).

The combined application of NR-I and NR-II, calculated with Eq. (11) using the parameters $\Gamma = 0.9$ and $(1-\Gamma) = 0.1$, is presented in Fig. 9(*d*). The combined approach resulted in a nucleation texture that includes $\alpha - fibre$ grains to a lesser extent, while maintaining a strong $\gamma - fibre$, conserving the higher intensities in the components $\{111\}\langle 123\rangle$ and $\{554\}\langle 225\rangle$. Additionally, the maximum intensity observed in the ODF from this combined method is $I_{max} = 19$, which is lower than the maximum intensities achieved through the separate applications of each nucleation rule, which were $I_{max} = 22$ and $I_{max} = 31$ for NR-I and NR-II, respectively. This result is closer to the maximum intensity observed for experimental nucleation texture $I_{max} = 10$, although there is still a discrepancy of a factor 2.

Furthermore, the texture shown in Fig. 9(*d*) includes $\alpha - fibre$ with $\Phi < 30°$, similar to those in Fig. 9(*c*), albeit at lower intensities. This feature matches the experimentally measured nucleation texture. However, components related to the $\theta - fibre$ and those with $\Phi >\sim 70°$, as observed in Fig. 9(*a*), are not predicted by either nucleation rule or their combination.

Main fibres volume fraction comparison

The simulated nucleation textures can also be compared with the experimentally estimated one by quantifying the volume fraction of the main crystallographic components. For this purpose, the four ODFs shown in Fig. 9 were partitioned considering the α, γ and θ fibres with a 15° tolerance from the ideal fibres. The results are shown in Fig. 10. In principle, it can be seen that all the nucleation textures contain orientations in the three crystallographic fibres, although some of them are not easy to visualise in the ODF plot. The $\gamma - fibre$ exhibited the highest volume fraction in each case, followed by the α and the $\theta - fibres$, except by the texture obtained with the exclusive application of SIBM nucleation (i.e. NR-II) which produced a $\theta - fibre$ with more than double the volume fraction of the $\gamma - fibre$. Furthermore, the nucleation texture resulting from the combined application of NR-I and NR-II displayed the closest volume fraction for the α and θ fibres relative to the experimental nucleation texture.

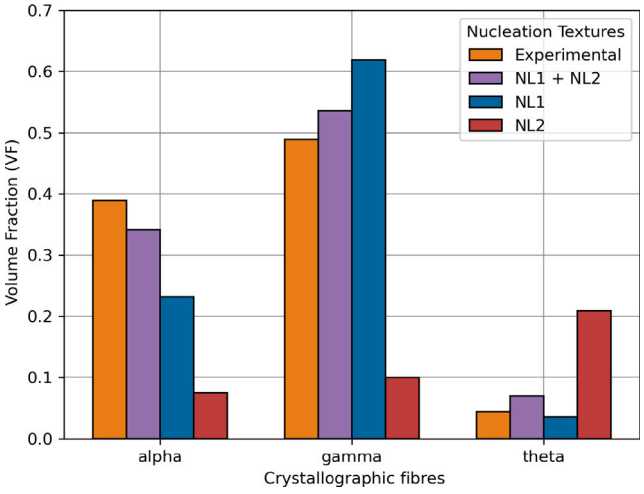

Fig. 10. Volume fraction for different crystallographic texture for the nucleation textures. Comparison with experimentally measured nucleation texture.

4. Discussion

Nucleation textures discrepancy

The deformation texture obtained from simulating a plane-strain compression deformation using the ALAMEL model was used to calculate nucleation textures derived from two nucleation rules and their combined effect. The first rule, NR-I, targets the nucleation of orientations with high stored energy, while the second rule, NR-II, selects orientations with low stored energy. Both rules employed the Taylor factor $M(g)$ to quantify the plastic energy accumulated during the rolling simulation. In NR-I, the nucleation probability is proportional to $M(g)$, whereas in NR-II, it is based on the difference in stored energy between paired grains (i, j), denoted as $\Delta M_{(i,j)}$. As detailed in Section 3.4, NR-I predominantly favours nucleation in the $\gamma - fibre$ region, associated with high stored energy, while NR-II enhances the nucleation in the $\alpha - fibre$, a region of low stored energy.

The comparison of the simulates nucleation textures with the experimentally estimated one reveals that some of the textures derived from the combined application of NR-I and NR-II correlate better with the experimental nucleation texture than the textures obtained solely through NR-I, as evidenced by the J_D correlation values presented Fig.

8. However, it is important to note that this observation does not apply to all simulation batches. This discrepancy may be partly due to the high rolling reduction of sample S_0. It is well-documented that the sub-grain coalescence nucleation mechanism, associated with NR-I, is predominant in heavily rolled low-carbon steels [7]. Since sample S_0 was subjected to an 80% reduction, the experimental nucleation texture from sample S_1 is expected to exhibit $\gamma - fibre$ orientations predominantly. Therefore, the contribution from the strain-induced boundary migration (SIBM) mechanism, activated by combining NR-I and NR-II, do not always improve the accuracy of the outcome when compared to the experimental nucleation texture.

On the other hand, Fig. 10 shows that the contribution of the $\theta - fibre$ orientations to the experimental nucleation texture is shallow. However, this result was not replicated in the texture calculated by combining NR-I and NR-II, where the $\theta - fibre$ contribution is higher than in the experimental case. The discrepancy suggests that while $\theta - fibre$ orientations contribute to the nucleation texture, their presence should be minimal. This represents a challenge for modelling the texture of early recrystallisation stages since it indicates that low-stored energy orientations must be included, but their selection cannot solely rely on stored-energy-based rules, as was assumed in this paper. Instead, additional criteria must be considered to ensure the appropriate selection of these low-stored energy orientations.

Nuclei distribution in Euler space

As shown in Fig. 7(d) the experimental nucleation texture predominantly exhibits a strong $\gamma - fibre(\langle 111\rangle \parallel ND)$. However, other crystallographic components within the Euler space zone defined by $0° < \phi_1 < 360°; 0° < \Phi < 30°; \phi_2 = 45°$ are also present, albeit at lower intensities. To analyse the presence of nuclei within this zone, the number distribution of nuclei in the Euler space for both textures, the experimentally measured and the one derived from the combined application of NR-I and NR-II are displayed in Fig. 11(a) and (b) respectively. This approach identifies the regions of Euler space occupied by the nuclei, independent of their volume fraction. To achieve this, the Euler space was segmented into a uniform grid with 5° intervals, referred to as boxes. Each nucleated orientation was allocated to the nearest box, with no overlapping orientations within the same box. This ensures that each recrystallised orientation is considered to have an equal volume fraction, with each counted only once in the ODF calculation. In this manner, the number ODF $f_n(g)$ was obtained by imposing a Gaussian functions with spread of $GS = 3°$ to enhance the visualisation of nuclei distribution within Euler space.

The number orientation distribution of nuclei in Euler space for the experimental nucleation texture is shown in Fig. 11(a). The preferred orientation of the nuclei in sample S_1 is predominantly around the $\gamma - fibre$, a trend that has been consistently reported in the literature [7,21,34]. Nuclei are also observed in the vicinity of the θ and α fibres, as well as others oriented significantly further from the ideal $\gamma - fibre$. Fig. 11(b) displays the orientation of nuclei in Euler space for the texture calculated by combining NR-I and NR-II. The orientation of the nuclei aligns with the experimental results, showing a primary preference for orientations around the $\gamma - fibre$. However, orientations in the $\alpha - fibre$ are also predicted by this model. Notably, the presence of nuclei with the rotated cube orientation, i.e., $\{001\}\langle 110\rangle$, is observed. This might be attributed to its low Taylor factor, which tends to result in a high absolute difference, denoted as $|\Delta M_{ij}|$, when paired with any other orientation during ALAMEL rolling simulation. As illustrated in Fig. 4, in NR-II, a higher $|\Delta M_{ij}|$ correlates with an increased probability of nucleation, provided that the high angle grain boundary (HAGB) criteria is met in accordance to Eq. (9).

The significant intensity of the rotated cube component depicted in Fig. 11(b) suggests that there may be a need to introduce a lower bound for stored energy in NR-II. This suggestion arises because, as demonstrated in Fig. 2, the rotated cube has the lowest Taylor Factor and yet it does not appear in the experimentally estimated nucleation texture. It is important to note that the Taylor factor M distribution in Euler space, shown in Fig. 2, was calculated using the Full-Constraints Taylor (FCT) model. In contrast, M values used in the simulations presented here were calculated with the ALAMEL model. In the ALAMEL model, the resulting M of each grain depends on its cluster assembly, cf. Fig. 1, whereas in the FCT model, the M is determine solely by the orientation g.

In addition, it can be noticed that the orientation of the predicted nuclei, Fig. 11(b), exhibits less dispersion compared to the orientation of the experimentally calculated nuclei, Fig. 11(a). This difference could be attributed to the ALAMEL's omission of grain fragmentation in its rolling simulations. Like other mean-field crystal plasticity models, such as the Full-Constraint model or Visco-plastic self-consistent model, the ALAMEL predicts deformation textures that lack information of the in-grain misorientation gradients [15]. Consequently, any nucleation texture derived from these deformation textures might fail to account for the orientation dispersion of the nuclei. In the context of mean-field modelling of recrystallisation textures, nucleation textures do not predict orientations absent from the deformation textures. Furthermore, grain fragmentation during deformation also contributes to the formation of high angle grain boundaries (HAGB) [35], which are essential for nucleation rules based on the SIBM mechanism, as the NR-II proposed in this paper.

Table 4
Chemical composition of *DC*04 steel cold rolled at 63%.

	C	Mn	Ti	N	Al
wt.[%]	0.044	0.0186	0.013	0.0052	0.0426

Analysis of sample rolled at lower percentage

To evaluate the model's performance at lower strain levels, a sheet of IF-steel with the chemical composition provided in Table 4 was also considered. It consisted of an industrially cold-rolled sheet with an approximately 63% reduction in thickness. Two samples were analysed: sample S_2, representing the deformed state, and an interrupted annealed sample, S_3, with approximately 11% recrystallised fraction, representing the nucleation state.

Similar to sample S_1, the EBSD data for sample S_3 was post-processed as described in Section 2.2.2 to obtain its nucleation texture. Fig. 12(a) presents the inverse pole figure map of the full EBSD dataset for sample S_3, while Fig. 12(b) highlights the nucleated grains, corresponding to ~10% recrystallised fraction. Fig. 12(c) and (d) show the textures (ODFs) of the coloured grains depicted in Fig. 12(c) and (d), respectively.

The texture in Fig. 12(c) exhibits the typical characteristics of a rolled BCC metal, specifically the presence of α and γ fibres, due to the high fraction of remaining deformed grains (~90%). In contrast, the texture in Fig. 12(d) is primarily characterised by the dominance of the γ-fibre. However, instead of being uniformly distributed as in sample $S_{!1}$ (c.f. Fig. 9(a)), it appears more dispersed across the orientation space. Additionally, some components traditionally associated with low Taylor factor values are observed above $\Phi = 30°$ and in $\{110\}\langle 001\rangle$, both displaying significant intensities. It is also important to note that some α-fibre components are present, though at lower intensities.

A second nucleation texture simulation was conducted to compare with the experimental results from sample S_3. The ALAMEL model was used to simulate plane strain compression at $\varepsilon = 1.0$, corresponding to a rolling reduction of ~63%. Due to the unavailability of EBSD data for the material in its undeformed state, a random texture was used as the initial texture, while all other rolling simulation settings remained unchanged from those described in Section 2.1.2. The resulting deformation texture is provided in Appendix B. The nucleation texture

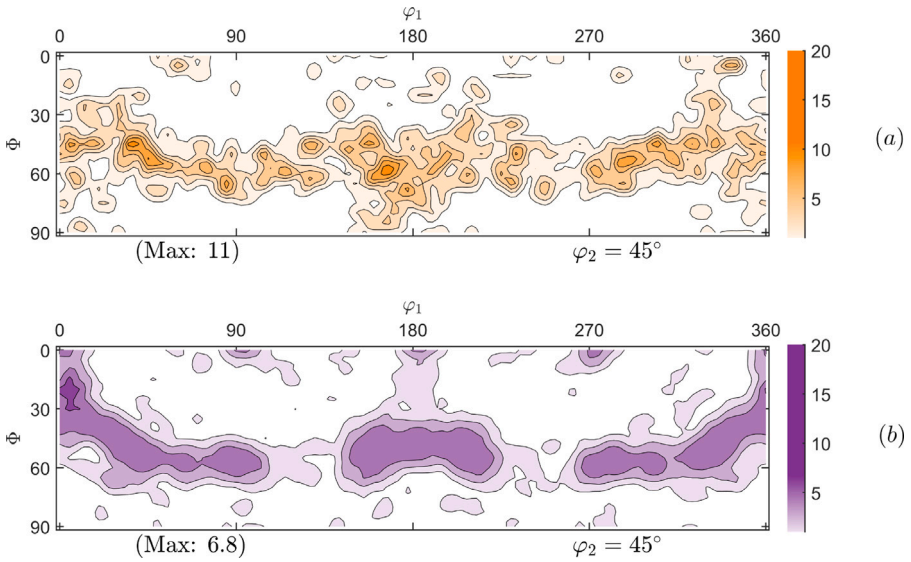

Fig. 11. Distribution of the nuclei in Euler space. (*a*) From calculated recrystallised fraction of sample S_1. (*b*) From predicted nucleation texture combining NR-I and NR-II, K–J nucleation and SIBM nucleation models respectively.

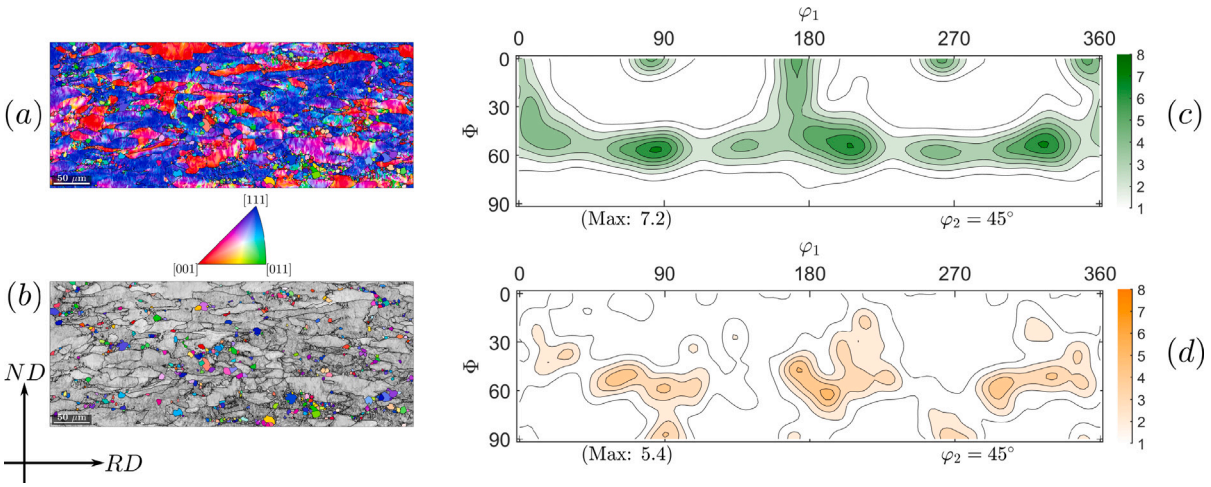

Fig. 12. IPF-map of the sample S_3, (*a*) all data and (*b*) early recrystallised grains. (*c*) Texture of the sample S_1 all grains (*d*) early recrystallised grains, it corresponds to the experimental nucleation texture in this study.

simulation was performed using NR-I with parameters $k_1 = 1.0$ and $M_0 = 80th - quantile$, and NR-II with parameters $a = 0.0$; $b = 1.0$; $c = [\max(M(g)) - \min(M(g))]/2$; $d = 6.0$ and $\theta_0 = 10.0°$. The combined effect of the NR-I and NR-II was obtained using $\Gamma = 0.9$ and $(1-\Gamma) = 0.1$. The obtained results are presented in Appendix B.

The orientation distribution of nuclei in Euler space for the experimental nucleation texture of sample S_3, along with the results of the second nucleation texture simulation, are presented in Fig. 13(*a*) and (*b*), respectively. The experimental results show a scattered distribution of nuclei along the γ−fibre and its surroundings, with a concentration of nuclei also present along the θ-fibre. In contrast, the simulated texture exhibits an almost uniform gamma-fibre distribution, along with some components in the θ-fibre, primarily the rotated cube component (i.e. $\{001\}\langle 010\rangle$) and a uniform α-fibre, with its highest intensity components located within this fibre.

An important observation is that the experimental results (cf. Fig. 13*a*) show nuclei concentrated between the α-fibre and α^*-fibre (cf. Fig. 5), while the simulated results display nuclei along the α-fibre (cf. Fig. 13*b*). Both regions are characterised by low Taylor factors for $\Phi < 40°$, which aligns with the objective of the SIBM nucleation model. However, the overestimation of components along the α-fibre is undesirable.

The origin of the overestimation of components on the α-fibre can be traced back to the simulated deformation texture generated by the ALAMEL model (see Appendix B). Since these components exhibit low Taylor factors, they are preferentially selected as high-probability

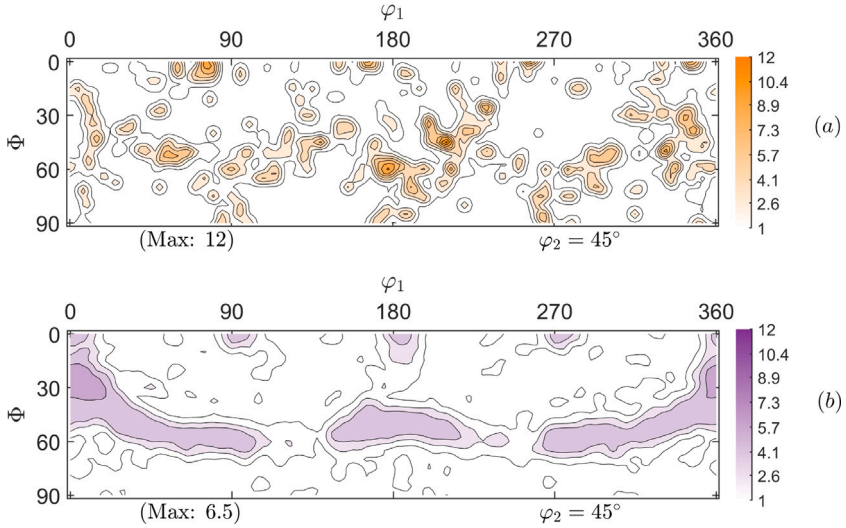

Fig. 13. Distribution of the nuclei in Euler space. (*a*) From calculated recrystallised fraction of sample S_2. (*b*) From predicted nucleation texture combining NR-I and NR-II is simulation 2.

nucleation sites. This finding reinforces the conclusion drawn from the simulation of sample S_1: that nucleation based solely on stored energy criteria is insufficient for accurately predicting nucleation texture.

5. Conclusions

This paper introduces a model to predict the nucleation texture of interstitial-free (IF) steel within a continuum modelling framework. The model integrates the effects of two nucleation rules, applied simultaneously using input from the Advanced-LAMEL model, a mean-field crystal plasticity model. The first rule, NR-I, is based on the Oriented Nucleation theory, which promotes the nucleation of orientations with high stored energy. The second rule, NR-II, is derived from the Strain-Induced Boundary Migration (SIBM) mechanism to favour the nucleation of orientations with low stored energy. The results demonstrate that NR-II favours the nucleation of orientations with low Taylor factor values, which in this study serve as an indirect measure of stored energy, leading to an nucleation textures that includes orientations within the α and θ crystallographic fibres. However, quantitative comparisons with the experimentally estimated from a sample at early recrystallisation stage reveal that the contribution of NR-II does not necessarily enhance the nucleation texture obtained solely through NR-I.

The findings of this study highlight two key points:

- NR-II may have overestimated low-stored energy orientations in the final nucleation texture, indicating the need to establish a lower-bound threshold for the Taylor factor when applying NR-II.
- Including α and θ fibres is important for enhancing the accuracy of the predicted nucleation texture. However, even if some orientations in these fibres share similar Taylor factor values, it does not necessarily mean that both should be included in the nucleation texture.

As a final remark, while a low Taylor factor is essential for nucleating low stored energy orientations, it should not be excessively low. Moreover, a low Taylor factor alone is insufficient for an orientation to be included in the nucleation texture.

CRediT authorship contribution statement

J. Ochoa-Avendaño: Writing – review & editing, Writing – original draft, Visualization, Validation, Software, Methodology, Investigation, Formal analysis, Data curation, Conceptualization. **C. Bos:** Writing – review & editing, Supervision, Software, Formal analysis, Conceptualization. **L.A.I. Kestens:** Writing – review & editing, Supervision, Formal analysis, Conceptualization.

Declaration of Generative AI and AI-assisted technologies in the writing process

During the preparation of this work the author(s) used OpenAI in order to improve the readability and language of the document. After using this tool/service, the author(s) reviewed and edited the content as needed and take(s) full responsibility for the content of the publication.

Declaration of competing interest

The authors declare the following financial interests/personal relationships which may be considered as potential competing interests: Jhon Ochoa-Avendano reports financial support was provided by M2i Materials Innovation Institute. If there are other authors, they declare that they have no known competing financial interests or personal relationships that could have appeared to influence the work reported in this paper.

Acknowledgements

This research was carried out under project number T17019f in the framework of the Partnership Programme of the Materials Innovation Institute M2i (www.m2i.nl). We would like to thank Tata Steel IJmuiden for providing the specimens, and to Monika Krugla for performing the EBSD experiments for this research. J. Ochoa-Avendaño gratefully acknowledges the Roberto Rocca Education Programme for its support.

Appendix A. Deformation texture evolution with ALAMEL model

ODFs of IF-steel. Initial texture ($\varepsilon = 0.0$) and ALAMEL model simulated deformation textures in plane strain compression at $\varepsilon = 0.22$, $\varepsilon = 0.51$, $\varepsilon = 0.91$, $\varepsilon = 1.6$ which correspond to 20%, 40%, 60% and 80% reduction respectively.

State	Texture
initial texture $\varepsilon = 0.0$	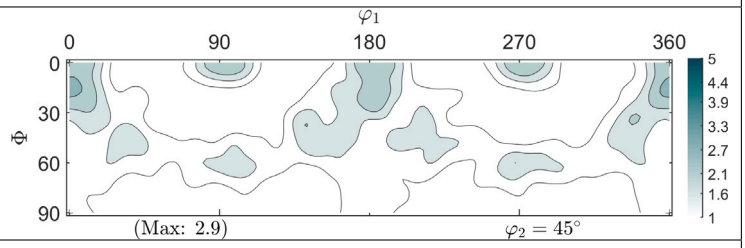
20% rolling reduction $\varepsilon = 0.22$	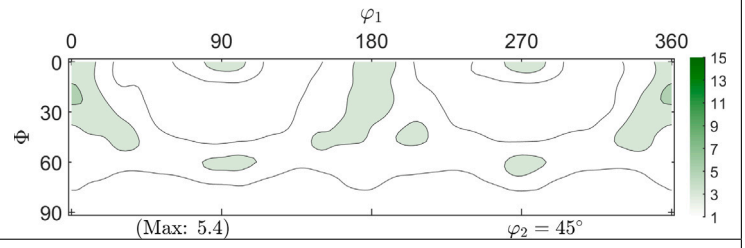
40% rolling reduction $\varepsilon = 0.51$	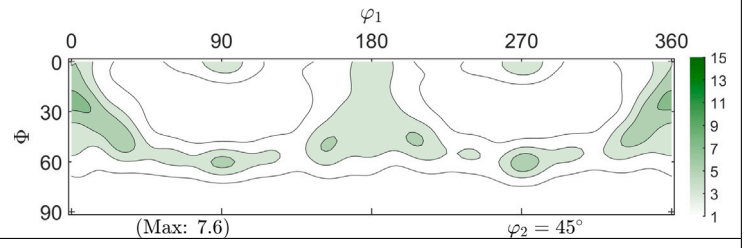
60% rolling reduction $\varepsilon = 0.91$	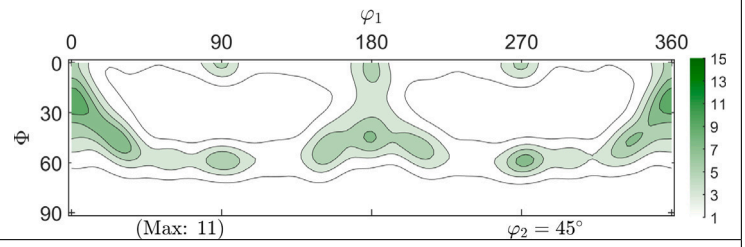
80% rolling reduction $\varepsilon = 1.41$	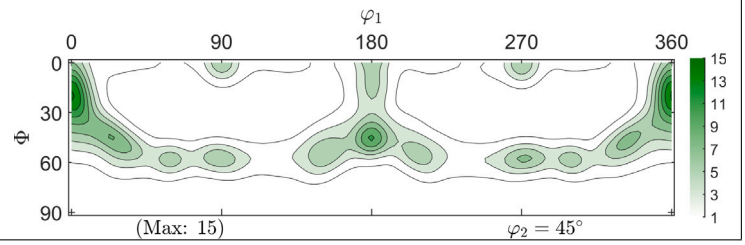

Appendix B. Results simulation 2

	Texture
Input texture for simulation	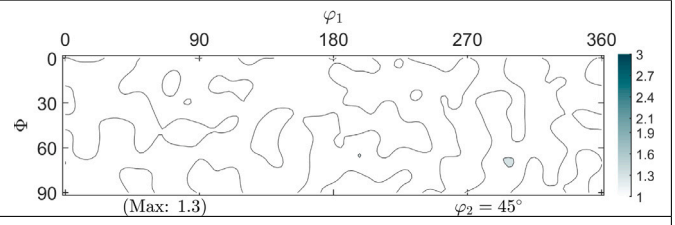
63% rolling reduction experimental	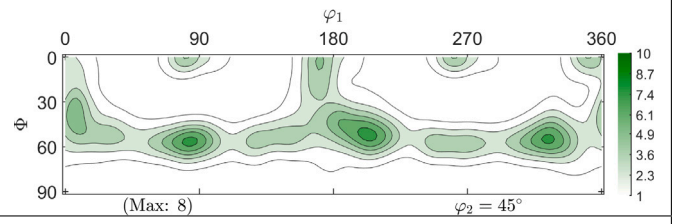
63% rolling reduction ALAMEL simulation	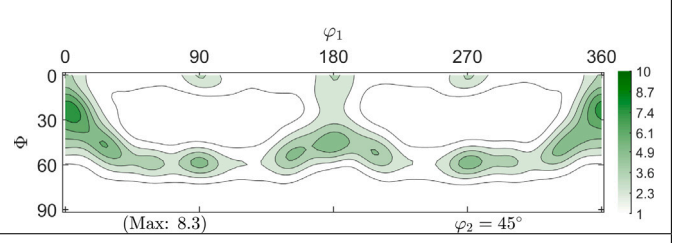
Nucleation texture K-J Model	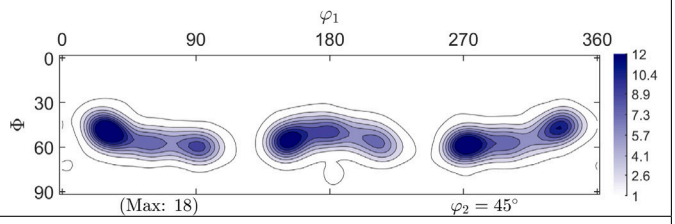
Nucleation texture SIBM Model	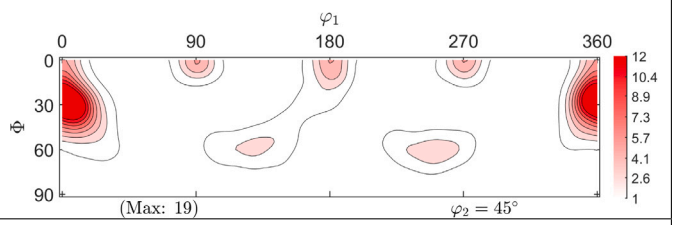
Nucleation texture Combining K-J Model and SIBM	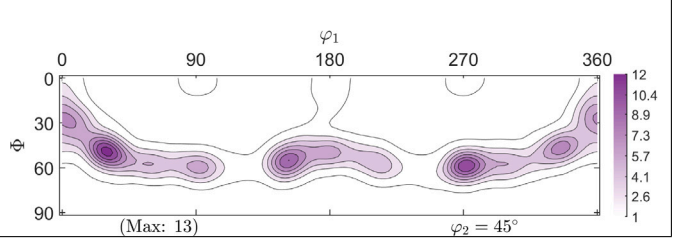

Data availability

The data that has been used is confidential.

References

[1] F. Humphreys, M. Hatherly, Chapter 12 - Recrystallization textures, in: F. Humphreys, M. Hatherly (Eds.), Recrystallization and Related Annealing Phenomena (Second Edition), second ed., Elsevier, Oxford, 2004, pp. 379–413, http://dx.doi.org/10.1016/B978-008044164-1/50016-5.

[2] L.A.I. Kestens, H. Pirgazi, Texture formation in metal alloys with cubic crystal structures, Mater. Sci. Technol. 32 (13) (2016) 1303–1315, http://dx.doi.org/10.1080/02670836.2016.1231746.

[3] M.M. Humane, R.K. Minz, R.K. Paretkar, D.R. Peshwe, Effect of cold rolling and mode of annealing on textures, mechanical properties and formability limit diagrams in interstitial free steel sheets, Trans. Indian Inst. Met. 63 (2010) 867–880, http://dx.doi.org/10.1007/s12666-010-0133-7.

[4] H.J. Bunge, U. Köhler, Modelling primary recrystallization in FCC and bcc metals by oriented nucleation and growth with the statistical compromise model, Textures Microstruct. 28 (1997) 1687–5397, http://dx.doi.org/10.1155/TSM.28.231.
[5] W.B. Hutchinson, Development and control of annealing textures in low-carbon steels, Int. Met. Rev. 29 (1) (1984) 25–42, http://dx.doi.org/10.1179/imtr.1984.29.1.25.
[6] U. Köhler, E. Dahlem-Klein, H. Klein, H.J. Bunge, Model calculations of recrystallization texture formation by growth selection, Textures Microstruct. 19 (1992) 1687–5397, http://dx.doi.org/10.1155/TSM.19.125.
[7] L. Kestens, J. Jonas, Modeling texture change during the static recrystallization of interstitial free steels, Met. Mater. Trans. A 27 (1) (1996) 1543–1940, http://dx.doi.org/10.1007/BF02647756.
[8] L. Kestens, J.J. Jonas, P. Van Houtte, E. Aernoudt, Orientation selective recrystallization of nonoriented electrical steels, Met. Mater. Trans. A 27 (8) (1996) 2347–2358, http://dx.doi.org/10.1007/BF02651889.
[9] J.J. Sidor, R.H. Petrov, L.A. Kestens, Modeling the crystallographic texture changes in aluminum alloys during recrystallization, Acta Mater. 59 (14) (2011) 5735–5748, http://dx.doi.org/10.1016/j.actamat.2011.05.050.
[10] A. Després, M. Greenwood, C. Sinclair, A mean-field model of static recrystallization considering orientation spreads and their time-evolution, Acta Mater. 199 (2020) 116–128, http://dx.doi.org/10.1016/j.actamat.2020.08.013.
[11] R. Quey, G. Fan, Y. Zhang, D. Juul Jensen, Importance of deformation-induced local orientation distributions for nucleation of recrystallisation, Acta Mater. 210 (2021) 116808, http://dx.doi.org/10.1016/j.actamat.2021.116808.
[12] E. Ferdinand Knipschildt, Nucleation of recrystallization, Mater. Sci. Technol. (United Kingdom) 38 (12) (2022) 765–779, http://dx.doi.org/10.1080/02670836.2022.2065054.
[13] P. Beck, P. Sperry, Strain induced grain boundary migration in high purity aluminum, J. Appl. Phys. 21 (2) (1950) 150–152, http://dx.doi.org/10.1063/1.1699614.
[14] C. Xu, Y. Zhang, A. Godfrey, G. Wu, W. Liu, J. Tischler, Q. Liu, D. Juul Jansen, Direct observation of nucleation in the bulk of an opaque sample, Sci. Rep. 7 (1) (2017) http://dx.doi.org/10.1038/srep42508.
[15] J. Ochoa-Avendaño, K. Sedighiani, J. Galan-Lopez, C. Bos, L. Kestens, Comparative analysis of crystal plasticity models in predicting deformation texture in IF-Steel, J. Mater. Res. Technol. 31 (2024) 3844–3859, http://dx.doi.org/10.1016/j.jmrt.2024.07.030.
[16] P. Van Houtte, S. Li, M. Seefeldt, L. Delannay, Deformation texture prediction: From the Taylor model to the advanced Lamel model, Int. J. Plast. 21 (2005) 589–624, http://dx.doi.org/10.1016/j.ijplas.2004.04.011.
[17] L.S. Tóth, P. Van Houtte, Discretization techniques for orientation distribution functions, Textures Microstruct. 19 (10.1155/TSM.19.229) (1992) 229–244.
[18] P. Bate, B. Hutchinson, A re-evaluation of the mechanism of SIBM, Scr. Mater. 36 (2) (1997) 195–198, http://dx.doi.org/10.1016/S1359-6462(96)00361-2.
[19] J. Cramer, The origins of logistic regression, SSRN Electron. J. 119 (4) (2002) 16, http://dx.doi.org/10.2139/SSRN.360300.
[20] P. Trusov, N. Kondratev, A.Y. A., A model for static recrystallization through strain-InducedBoundary migration, Phys. Mesomech. 23 (2) (2020) 97–108, http://dx.doi.org/10.1134/S1029959920020010.
[21] A. Ayad, M. Ramoul, A. Rollett, F. Wagner, Quantifying primary recrystallization from EBSD maps of partially recrystallized states of an IF steel, Mater. Charact. 171 (2021) 110773, http://dx.doi.org/10.1016/j.matchar.2020.110773.
[22] J. Tarasiuk, P. Gerberand, B. Bacroix, Estimation of recrystallized volume fraction from EBSD data, Acta Mater. 50 (6) (2002) 1467–1477, http://dx.doi.org/10.1016/S1359-6454(02)00005-8.
[23] S. Dziaszyk, E. Payton, F. Friedel, V. Marx, G. Eggeler, On the characterization of recrystallized fraction using electron backscatter diffraction: A direct comparison to local hardness in an IF steel using nanoindentation, Mater. Sci. Eng.: A 527 (29) (2010) 7854–7864, http://dx.doi.org/10.1016/j.msea.2010.08.063.
[24] D.P. Field, Quantification of partially recrystallized polycrystals using electron backscatter diffraction, Mater. Sci. Eng.: A 190 (1) (1995) 241–246, http://dx.doi.org/10.1016/0921-5093(94)09601-R.
[25] M. Sanjariand, M. Mehdi, Y. He, E. Hilinski, S. Yue, L. Kestens, A. Edrisy, Tracking the evolution of annealing textures from individual deformed grains in a cross-rolled non-oriented electrical steel, Met. Mater. Trans. A 48 (12) (2017) 1543–1940, http://dx.doi.org/10.1007/s11661-017-4370-9.
[26] M. Diehl, L. Kertsch, K. Traka, D. Helm, D. Raabe, Site-specific quasi in situ investigation of primary static recrystallization in a low carbon steel, Mater. Sci. Eng.: A 755 (2019) 295–306, http://dx.doi.org/10.1016/j.msea.2019.02.032.
[27] P. Orsetti Rossi, C. Sellars, Quantitative metallography of recrystallization, Acta Mater. 45 (1) (1997) 137–148, http://dx.doi.org/10.1016/s1359-6454(96)00167-x.
[28] D. Mainprice, F. Bachmann, R. Hielscher, H. Schaeben, Mtex documentation, 2024, URL: https://mtex-toolbox.github.io/Documentation.
[29] F. Bachmann, R. Hielscher, H. Schaeben, Texture analysis with MTEX, free and open source software toolbox, in: Texture and Anisotropy of Polycrystals III, in: Solid State Phenomena, vol. 160, Trans Tech Publications Ltd, 2010, pp. 63–68, http://dx.doi.org/10.4028/www.scientific.net/SSP.160.63.
[30] H. Bunge, 3 - Orientation distributions, in: H. Bunge (Ed.), Texture Analysis in Materials Science, Butterworth-Heinemann, 1982, pp. 42–46, http://dx.doi.org/10.1016/B978-0-408-10642-9.50008-8.
[31] B. Beausir, J.-J. Fundenberger, Atex-software analysis tools for electron and x-ray diffraction, 2017.
[32] M. Zecevic, R.A. Lebensohn, R.J. McCabe, M. Knezevic, Modeling of intragranular misorientation and grain fragmentation in polycrystalline materials using the viscoplastic self-consistent formulation, Int. J. Plast. 109 (2018) 193–211, http://dx.doi.org/10.1016/j.ijplas.2018.06.004.
[33] D. Kim, W. Woo, W. Park, Y. Im, A. Rollett, Mesoscopic coupled modeling of texture formation during recrystallization considering stored energy decomposition, Comput. Mater. Sci. 129 (2017) 55–65, http://dx.doi.org/10.1016/j.commatsci.2016.11.048.
[34] B. Hutchinson, D. Artymowicz, Mechanisms and modelling of microstructure/texture evolution in interstitial-free steel sheets, ISIJ Int. 41 (6) (2001) 533–541, http://dx.doi.org/10.2355/isijinternational.41.533.
[35] D. Hughes, N. Hansen, High angle boundaries formed by grain subdivision mechanisms, Acta Mater. 45 (9) (1997) 3871–3886, http://dx.doi.org/10.1016/S1359-6454(97)00027-X.